

Assesment of zonal symmetric and asymmetric components of the Southern Annular Mode using a novel approach

Elio Campitelli * and Leandro B. Díaz

*Universidad de Buenos Aires, Facultad de Ciencias Exactas y Naturales, Departamento de
Ciencias de la Atmósfera y los Océanos, Buenos Aires, Argentina CONICET – Universidad de
Buenos Aires, Centro de Investigaciones del Mar y la Atmósfera (CIMA), Buenos Aires, Argentina
CNRS – IRD – CONICET – UBA, Instituto FrancoArgentino para el Estudio del Clima y sus
Impactos (UMI 3351 IFAECI), Buenos Aires, Argentina*

Carolina Vera

*Corresponding author: Elio Campitelli, elio.campitelli@cima.fcen.uba.ar

ABSTRACT

11 Enter the text of your abstract here. This is a sample American Meteorological Society (AMS)
12 \LaTeX template. This document provides authors with instructions on the use of the AMS \LaTeX tem-
13 plate. Authors should refer to the file `amspaper.tex` to review the actual \LaTeX code used to create
14 this document. The `template.tex` file should be modified by authors for their own manuscript.

15 *Significance statement.* This is significant because I wrote it.

16 **1. Introduction**

17 The Southern Annular Mode (SAM) is the main mode of variability in the Southern Hemisphere
18 extratropical circulation (Rogers and van Loon 1982) in daily, monthly, and decadal timescales
19 (Baldwin 2001; Fogt and Bromwich 2006) and exerts an important influence in weather conditions
20 such as temperature and precipitation anomalies and sea ice concentration (Fogt and Marshall
21 2020). Its positive phase is traditionally described as anomalously low pressures over Antarctica
22 surrounded by a ring of anomalous high pressures in middle-to-high latitudes.

23 Most authors describe the SAM as a zonally symmetric pattern, a fact that is reflected not only
24 in its name, but also in the various methods used to characterise it. Of the several different
25 indices presented in the literature, many of them are based on zonal means of sea level pressure or
26 geopotential height (Ho et al. 2012). Gong and Wang (1999) defined the SAM index as the zonal
27 mean sea level pressure difference between 40°S and 60°S, which is also the definition used by
28 the station-based index in Marshall (2003). Baldwin and Thompson (2009) proposed defining the
29 Northern and Annular modes as the leading EOF of the zonally averaged geopotential height at
30 each level.

31 Even though these indices are based on zonal averages, the spatial the spatial structure of the
32 SAM computed from them contains noticeable deviations from zonal symmetry, particularly in the
33 Pacific Ocean region. These zonal asymmetries have not been widely studied, but previous work
34 suggest that they strongly modulate the regional impacts of the SAM, going as far as reversing
35 its relationship between precipitation in South America (Silvestri and Vera 2009). At the very
36 least, the fact that the SAM is not entirely zonally symmetric hinders our ability to reconstruct its

37 historical variability prior to the availability of dense observations in the Southern Hemisphere
38 (Jones et al. 2009).

39 At least some of the variability associated with the zonal asymmetries of the SAM is probably
40 forced by the tropics. In particular, ENSO-like variability affects the Southern Hemisphere ex-
41 tratropics through the Pacific-South American Pattern (Mo and Ghil 1987; Kidson 1988; Karoly
42 1989), whose wave train projects strongly onto the zonal anomalies corresponding to the SAM
43 in the Pacific sector. And although the relationship between ENSO and SAM is far from simple,
44 tropical influences on the SAM have been observed (Fan 2007; Fogt et al. 2011; Clem and Fogt
45 2013). In particular, Fan (2007) computed SAM indices of the Western and the Eastern Hemi-
46 sphere separately and found that they were much more correlated if the (linear) signal of the ENSO
47 was removed. While this relates to temporally coherent variability of the two hemisphere and not
48 necessarily to zonal asymmetries in the associated spatial patterns, it is nonetheless consistent of
49 the ENSO playing a crucial role in zonal asymmetries of the SAM.

50 Positive trends in SAM index have been documented by various researchers using different
51 indices mostly on boreal Summer and Autumn (Fogt and Marshall 2020, and references therein).
52 These trends are thought of driven primarily by stratospheric ozone depletion and understood in
53 the context of zonal mean variables. However, it's not clear how or if the asymmetric component
54 responds to this forcing, or whether its variability could be masking influencing the observed trends
55 independently.

56 Similarly unclear are the specific impacts of the zonally asymmetric component of the SAM.
57 Positive phase of the SAM is associated with generally colder temperatures over Antarctica and
58 warmer temperatures at higher latitudes (Jones et al. 2019) (and vice versa for negative SAM), but
59 there are significant deviations from this zonal mean response, notably in the Antarctic Peninsula
60 and the South Atlantic (Fogt et al. 2012). The SAM signal in precipitation behaves similarly,

61 although with even greater deviation from zonal symmetry (Lim et al. 2016). The importance of
62 zonal asymmetries of the SAM in these impacts have been studied in certain regions. For example,
63 the SAM-precipitation relationship in Southeastern South America and Southern Brazil can be
64 explained by the PSA-like zonally asymmetric circulation associated with the SAM (Silvestri and
65 Vera 2009; Rosso et al. 2018). Fan (2007) also found that precipitation in East Asia was impacted
66 by the variability of only the Western Hemisphere part of the SAM.

67 We are not aware of any previous work which quantifies the temporal variability of the asymmetric
68 component of the SAM with the exception of Fogt et al. (2012). However, their methods based
69 on composites of positive and negative SAM events leads to some issues, such as spatial patterns
70 derived from as little as 4 cases and from imbalanced periods (for example, 5 of the 7 cases in
71 their DJF SAM+ composite are from later than 1988, whereas all of the 8 years in their DJF SAM-
72 composite are from earlier than 1988). This is particularly important due to the inhomogeneities
73 in reanalysis products prior to the satellite era and the possible change in the asymmetric structure
74 of the SAM (Silvestri and Vera 2009).

75 Moreover, Fogt et al. (2012) studied the zonal asymmetric component of the SAM only in sea
76 level pressure. Zonal asymmetries in the SAM spatial pattern are fairly barotropic throughout the
77 troposphere, but they change dramatically in the stratosphere (Baldwin and Thompson 2009).

78 Our objective is, then, to systematically characterise the zonally asymmetric and symmetric
79 components of the SAM variability. For each level, we construct two indices which aim to
80 capture exclusively the variability of the symmetric and asymmetric component respectively. We
81 assess their vertical structure and coherence, temporal variability and trends. We then study the
82 spatial patterns described by the variability exclusive to each index. Finally, we investigate their
83 relationship with temperature and precipitation anomalies.

84 In the Section 2 we describe the methods. In Section 3.a we describe the temporal variability
85 and vertical coherence of the indices. In Section 3.b, we analyse the spatial patterns of geopo-
86 tential height associated with them. In Section 3.c, we study their relationship with surface-level
87 temperature and precipitation.

88 **2. Methods**

sec:methods

89 **1) DATA**

90 To describe the Southern Annular Mode and its variability we used monthly geopotential height
91 at 2.5° longitude by 2.5° latitude of horizontal resolution and 37 vertical isobaric levels from ERA5
92 (Hersbach et al. 2020) for the period 1979 to 2018. We restrict our analysis to the post-satellite era
93 to avoid any confounding factors arising from the introduction of satellite observations.

94 To describe the relationship between the SAM indices and temperature and precipitation, we use
95 temperature data from NOAA's Merged Land Ocean Global Surface Temperature Analysis V4.0.1
96 (Vose et al. 2012; Smith et al. 2008), which blends land and ocean temperature analysis into a
97 monthly global grid 5° longitude by 5° latitude, and monthly rainfall 0.5° longitude by 0.5° latitude
98 data from the Global Precipitation Climatology Centre (Schneider et al. 2015).

99 **2) DEFINITION OF INDICES**

100 Traditionally the Souther Annular Mode (SAM) is defined as de leading Empirical Orthogonal
101 Mode (EOF) of sea level pressure or geopotential height at lower levels (Ho et al. 2012). Following
102 Baldwin and Dunkerton (2001), we extend that definition vertically and use the term SAM to refer
103 to the the leading EOF of the monthly anomalies of geopotential field south of 20°S at each level.
104 We performed EOFs by computing the Singular Value Decomposition of the data matrix consisting
105 in 481 rows and 4176 columns (144 points of longitude and 29 points of latitude). We weighted

106 the values by the square root of the cosine of latitude to account for the non-equal area of each
107 gridpoint (Chung and Nigam 1999).

108 To separate the zonally symmetric and asymmetric components of the SAM, we computed
109 the zonal mean and anomalies of the full SAM spatial pattern, as shown in Figure 1 for 700
110 hPa. The full spatial signal ($\text{EOF}_1(\lambda, \phi)$) is the sum of the zonally asymmetric ($\text{EOF}_1^*(\lambda, \phi)$) and
111 symmetric ($[\text{EOF}_1](\lambda, \phi)$) components. We then compute the “Full SAM”, “Asymmetric SAM”
112 and “Symmetric SAM” indices as the regression coefficients of the regression of each monthly
113 geopotential field on the respective patterns (weighting by the cosine of latitude). The three indices
114 are normalized by dividing them by the standard deviation of the “Full” index at each level. As a
115 result, the magnitudes between indices are comparable. However, only “Full” index will have unit
116 standard deviation per definition. From the regression, we also use the explained variance of each
117 pattern as an indicator of the degree of zonally symmetry or asymmetry of each monthly field.

118 Our method assumes linearity in the asymmetric component of the SAM. That is, we assume that
119 zonal symmetries associated with positive SAM are almost opposite and of the same magnitude
120 to the ones associated with negative SAM. Fogt et al. (2012)’s composites (their Figure 4) suggest
121 that this might not be entirely valid, although we argue that much of that apparent non-linearity
122 is due to the heterogenous nature of the selected years for constructing the composites. Using
123 our data (from 1979 to 2018), seasonal composites of zonal anomalies of 700 hPa geopotential
124 height for SAM+ (Full SAM index greater than 1 standard deviation) and SAM- (less than minus
125 1 standard deviation) show relatively high pattern correlations for all seasons and are visually very
126 linear (Figure A9). Therefore, we believe that our method is a reasonable approximation of the
127 phenomenon.

128 By computing a single EOF pattern using data for all months we are assuming that the zonal
129 anomalies of the SAM are the same in all seasons –December to February (DJF), March to May

(MAM), June to August (JJA) and September to November (SON). Geopotential zonal anomalies computed by projecting the first EOF *of each season* are very similar to each other (Figure A10) and show pattern correlations between 0.65 (DJF with JJA) and 0.9 (between MAM and SON). Based on this, we believe that our initial assumption is not unreasonable.

Finally, we assume that the zonally asymmetric pattern is stationary in time. Silvestri and Vera (2009) suggest that this might not be the case between 1958 and 2004 but the period we analyse is much shorter (1979-2018) so it's unlikely that we could observe significant changes. Moreover, zonal asymmetry of the spatial patterns for the two halves of the period (1979 to 1998 and 1999 to 2018) show no systematic change (Figure A11).

3) REGRESSIONS

We perform linear regressions to quantify the association between the SAM indices and other variables. Since the Asymmetric and Symmetric SAM indices are significantly correlated with each other, to capture the variability explained uniquely by each index we use one multiple linear regression instead of two simple linear regressions. To obtain the linear coefficients of a variable X (geopotential, temperature, precipitation, etc...) with the Asymmetric SAM (SAM_a) and Symmetric SAM (SAM_s) we fit the equation

$$X(\lambda, \phi, t) = \alpha(\lambda, \phi)SAM_a + \beta(\lambda, \phi)SAM_s + X_0(\lambda, \phi) + \epsilon(\lambda, \phi, t)$$

where λ and ϕ are the longitude and latitude, t is the time, α and β are the linear regression coefficients, X_0 and ϵ are the constant and error terms. From this equation, α represents the (linear) association of X with the variability of the Asymmetric SAM that is not explained by the variability of the Symmetric SAM; i.e. it is proportional to the partial correlation of X and the Asymmetric SAM, controlling for the effect of the Symmetric SAM and vice versa for β . When performing a

151 separate regression for each trimester (DJF, MAM, JJA, SON), we average of the relevant variables
152 seasonally for each year and trimester before computing the regression.

153 At 2.5°by 2.5°resolution, a single regression field is composed of thousands of regressions. In
154 such case, using p-values to test for significance leads to misleading results (Walker 1914; Katz and
155 Brown 1991). While there are multiple proposed solutions in the literature, Wilks (2016) suggests
156 that adjusting p-values by controlling for the False Discovery Rate (Benjamini and Hochberg 1995)
157 is a simple and effective method to ameliorate this issue. Therefore, p-values showed in regression
158 fields are all adjusted following Benjamini and Hochberg (1995).

159 We computed linear trends by Ordinary Least Squares and the 95% confidence interval assuming
160 a t-distribution of the appropriate residual degrees of freedom.

161 To compute the amplitude of the zonal waves we computed the Fourier transform of the spatial
162 field at each latitude circle.

163 4) COMPUTATION PROCEDURES

164 We performed all analysis in this paper using the R programming language (R Core Team 2020),
165 using the data.table package (Dowle et al. 2020) and the metR package (Campitelli 2020). All
166 graphics are made using ggplot2 (Wickham 2009). We downloaded data from ranalysis using the
167 ecmwfr package (Hufkens et al. 2020) and indices of the ENSO with the rsoi package (Albers and
168 Campitelli 2020). The paper was rendered using knitr and rmarkdown (Xie 2015; Allaire et al.
169 2019).

170 A version-controlled repository of the code used to create this analysis can be found at
171 <https://github.com/eliocamp/asymsam>.

3. Results

sec:results

a. Temporal evolution

sec:temporal

We first assess the temporal evolution of the Asymmetric SAM and Symmetric SAM. Figure 2 shows the corresponding time series for 700 hPa and 50 hPa and their corresponding density estimates. We selected these two levels as representative of the tropospheric and stratospheric variability respectively. As will be shown later, both indices are highly coherent within each atmospheric layer, therefore it is reasonable to take one level as representative of each layer.

Month-to-month variability is evident for both indices, with noisy variations in the low frequency. At first glance the series can be distinguished by their distributions. Compared to the tropospheric indices, the stratospheric indices are much more long-tailed; that is, extreme values (both negative and positive) abound. The Asymmetric SAM series have both more variability in the higher frequencies than the Symmetric SAM series.

The stratospheric Symmetric SAM varies strongly with a two-year period, which can be seen by spectral analysis (Figure A3). This might suggest a link between stratospheric SAM variability and the Quasi-Biennial Oscillation (Baldwin et al. 2001). There is a local peak at 2 years in the periodogram of the tropospheric Symmetric SAM also, although it's not statistically significant. In the troposphere the most significant peak of variability is found in the Asymmetric index at around 3.6 months.

From Figure 2 we can see that the Asymmetric SAM and Symmetric SAM time series appear to be correlated. Moreover, looking at the extremes in the stratosphere, the Symmetric SAM series appears to lag the Asymmetric SAM series (see, for example, the positive events on late 1987). We show these correlations, across all the levels of the reanalysis for zero and -1 lag (Asymmetric SAM index leading the Symmetric SAM index), in Figure 3. Zero-lag correlations

195 between the Asymmetric SAM and Symmetric SAM series are relatively constant throughout
196 the troposphere, fluctuating between 0.39 and 0.45. One-month-lag correlations are similarly
197 constant but significantly reduced to around 0.17. In the stratosphere, zero-lag correlations drop
198 to a minimum of 0.21 at 20 hPa and then it increases again monotonically with height up to the
199 uppermost level of the reanalysis (although results near the top of the models are to be interpreted
200 with care). At the same time, one-month-lag correlations increase with height. As a consequence,
201 stratospheric Asymmetric SAM index tend to precede corresponding Symmetric SAM index.

202 Figure 4a shows (zero-lag) cross-correlation across levels for the Full, Symmetric and Asym-
203 metric SAM indices. For the Full SAM (panel a), high values below 100 hPa reflect the vertical
204 (zero-lag) coherency throughout the troposphere. Above 100 hPa correlation between levels falls
205 off more rapidly, indicating less coherent (zero-lag) variability. Therefore, there is a non negligible
206 correlation between the troposphere and the lower-to-middle stratosphere. Examining panels b and
207 c, we see that the Asymmetric and Symmetric SAM share the same high level of coherency in the
208 troposphere but they differ in their stratospheric behaviour. Stratospheric coherency is stronger
209 for the Asymmetric SAM than the Symmetric SAM. The stratospheric Symmetric SAM seems to
210 connect more strongly to the troposphere than the Asymmetric SAM.

211 The linear trends for each of the indices (Full SAM, Symmetric SAM and Asymmetric SAM)
212 were evaluated for the complete period 1979-2018 at each level (Figure 5) for the whole year and
213 separated by trimesters. The Full SAM index presents a statistically significant trend (panel a.1)
214 that extends throughout the troposphere up to about 50 hPa and reaches its maximum value at 100
215 hPa. The seasonal trends (rest of column a) indicate that positive trends are present in Autumn
216 and particularly in Summer, where the 100 hPa maximum is much more defined. In Winter and
217 Spring, we detect no statistically significant trend. This is consistent with the results of previous
218 studies, which find clear positive trends in Summer, weaker in Autumn and no trends in the other

seasons (e.g. Fogt and Marshall 2020, and references therein) using indices of the SAM based on surface or near-surface circulation.

By separating the SAM signal in its asymmetric and symmetric parts, we can not only see that these trends are almost entirely due to the symmetric component (column b vs. column c), but in some cases the trends become more clear. In Summer, the Asymmetric SAM has a statistically non significant negative trend in the middle troposphere that obscures the trend in the Full SAM index; as a result, trends computed using only the Symmetric component are more clear (compare the shading region in panel a.2 and c.2). In Autumn, the Symmetric SAM reveals a statistically significant positive trend in the stratosphere that is not significant using the Full SAM index.

We stress that these are only linear trends during the whole period and the absence of a statistically significant signal should not be taken as evidence of no systematic change. In particular, going back to Figure 2, we can see an evident change in the stratospheric Asymmetric component (red line in panel a) between the 90's, when we see a dominance of extreme negative values, and the 00's, when we see the inverse. This change is restricted to the Winter months: the linear trend for Winter starting in 1990 for the Asymmetric component at 50hPa is 0.37 ± 0.22 .

Figure 6 shows decadal trends for the explained variance of each index. There is no evidence of a significant trend in the stratosphere. In the troposphere, there is a positive trend for the Asymmetric SAM and not significant trend for the Symmetric SAM. This suggest that the SAM has become more asymmetric in the period from 1979 to 2018. However, the change is slight, around 1% increased explained variance per decade.

b. Spatial patterns

sec:spatial

To show if, and to what extent, the Asymmetric and Symmetric SAM indices indeed capture the asymmetric and symmetric component of the SAM respectively, we computed the spatial

242 regression of geopotential height anomalies on these indices and the Full SAM index for 700 hPa
243 and 50 hPa levels. Figure 7 shows these regressions. Regression coefficients in column a are
244 computed using the Full SAM. Regression coefficients in columns b and c are computed using
245 multiple regression using the Asymmetric and Symmetric indices at the same time. Thus, they
246 are to be interpreted as the patterns associated with each index, removing the variability (linearly)
247 explained by the other index.

248 In the stratosphere, the spatial pattern associated with the Full SAM is more clearly dominated
249 by a zonally symmetric, monopolar structure (panel a.1) which is, however, not perfectly centred in
250 the South Pole. The monopole obtained by the regression pattern for Symmetric SAM (panel c.1)
251 is much more symmetric and the shift from total symmetry is captured by the regression pattern of
252 the Asymmetric SAM as a wave-1 with maximum anomalies above the Belinghausen Sea on the
253 Western Hemisphere and Davis Sea in the Eastern Hemisphere (panel b.1).

254 In the troposphere, panel a.2 shows the well known combination of zonally symmetrical an-
255 nular mode with zonal asymmetries in the form of a wave-3 (Fogt et al. 2012). The regression
256 using the Asymmetric and Symmetric SAM indices successfully disentangle both structures. The
257 Asymmetric SAM index gives rise to a cleaner zonal wave (panel b.2) and the Symmetric SAM
258 index is associated with an annular mode, almost devoid of zonal asymmetries (panel c.2). The
259 wave-3 pattern observed in panel b.2 is rotated by half a wavelength from the average position of
260 the mean wave-3 pattern associated with Raphael (2004)'s ZW3 index, whose reference locations
261 are marked with points in the figure. Thus, the tropospheric Asymmetric SAM index represents a
262 zonal displacement in the position of the climatological wave-3 pattern.

263 The amplitude of the first zonal wave numbers at each latitude at 50 hPa and 700 hPa is shown
264 in Figure 8, where wave number zero represents the amplitude of the zonal mean. Zonal wave
265 amplitudes of the spatial pattern described by the Full SAM index (column a) are dominated by

the zonal mean (wave-number 0) at both levels. However, zonal waves are important, particularly North of 50°S, with wave-number 1 clearly dominating at 50 hPa (panel a.1) and a more equal mix of waves at 700 hPa (panel a.2). Column b shows that the Asymmetric SAM is overwhelmingly dominated by wave 1 in the stratosphere (panel b.1), while in the troposphere it is composed of zonal waves 3 to 1 in decreasing level of importance (panel b.2) with negligible amplitude of the zonal mean. The Symmetric SAM, on the other hand, it's almost entirely composed of zonal mean at both levels (column c), with little to now contribution from zonal waves with wave-numbers 1 to 3.

We can see that the amplitude and latitudinal distribution zonal waves in the Asymmetric SAM on one hand, and the zonal mean in the Symmetric SAM on the other correspond almost exactly to the amplitude and latitudinal distribution in the Full SAM. This confirms the correct decomposition of the SAM in its symmetric and asymmetric components.

Looking at panel b.2 from Figure 7, it becomes apparent that zonal waves 1 and 2 modulate the amplitude of zonal wave 3, which –as mentioned before– is larger in the Western Hemisphere than in the Eastern Hemisphere.

To analyse the vertical structure of the geopotential height anomalies associated with the asymmetric SAM index, we show a vertical cross section of regressions of mean geopotential height between 65°S and 40°S for the 50 hPa Asymmetric SAM index (panel a) and for the 700 hPa Asymmetric SAM index (panel b) (Figure 9). The geopotential height anomalies associated with the stratospheric Asymmetric SAM (panel a) are clearly constrained to the stratosphere, which underscores the uncoupling between the stratospheric and tropospheric Asymmetric SAM. The vertical structure of this signal tilts about 60° to the West between 100 hPa and 1 hPa, suggesting baroclinic processes. Interestingly, the signal in the stratosphere maximises near 10 hPa despite using the 50 hPa index for the regression.

290 The tropospheric Asymmetric SAM (panel b) has significant signals that extend upwards to
 291 the uppermost levels of the reanalysis. In the troposphere, the wave-3 structure is equivalent
 292 barotropic with maximum amplitude at roughly 250 hPa. The anomalies are much more intense
 293 in the Western hemisphere, where they extent into the stratosphere. In the Eastern hemisphere the
 294 wave-3 signal is weaker and confined to the troposphere while negative anomalies dominate in the
 295 stratosphere. So, while the tropospheric Asymmetric SAM index is associated with stratospheric
 296 geopotential anomalies, these do not project strongly onto the stratospheric Asymmetric SAM.
 297 The structures shown in panels a and b in Figure 9 are robust to the choice of index level. For
 298 any stratospheric (above 100 hPa) index, the resulting anomalies are very similar to the wave-1
 299 structure with maximum near 10 hPa in panel a. Conversely, for any tropospheric (below 100 hPa)
 300 index, the result is very similar to panel b. The patterns mainly change in amplitude (not shown).

301 The wave-3 pattern from Figure 7 panel b.2 is very similar to the Pacific-South American Pattern
 302 (Mo and Ghil 1987; Kidson 1988) which is a teleconnection pattern associated with the ENSO
 303 (Karoly 1989). Indeed, Fogt et al. (2011) showed that there is a significant relationship between
 304 the SAM and the ENSO. The correlation between the Full SAM and the ENSO as measured by
 305 the Oceanic Niño Index (Bamston et al. 1997) (ONI) is -0.16 (p-value = 2.8×10^{-4}). Consistent
 306 with Fan (2007), we show that this relationship is captured entirely by the Asymmetric SAM, as
 307 this index has a partial correlation of -0.26 (p-value = 6.3×10^{-9}) with the ONI controlling for the
 308 effect of the Symmetric SAM, whereas the Symmetric SAM's partial correlation with the ONI is
 309 essentially null (0.019; p-value = 0.67). We performed the same analysis using the Multivariate
 310 ENSO Index (Wolter and Timlin 2011) and the Southern Oscillation Index (Ropelewski and Jones
 311 1987) to conclude that these results do not depend on the ENSO index used.

To see if there are different surface impacts associated with the asymmetric and symmetric SAM circulation we regress surface temperature and precipitation onto each of the three SAM indices at 700 hPa. As shown in previous sections, the three indices are highly coherent in the troposphere, so we select this level to represent the tropospheric circulation for consistency with previous studies.

Figure 10 shows regression coefficients of each index at 700 hPa with surface temperature for each trimester. In Summer, positive values of the Full SAM index (panel a.1) are associated with negative temperature anomalies near Antarctica which are surrounded by a ring of positive anomalies. The ring is not zonally symmetric, as there are four clear local maximums around 30°W, 120°W, 150°E and 90°E. In the tropics, there are negative anomalies in the equatorial Pacific, consistent with the negative correlation between SAM and ENSO. Panels b.1 and c.1 show temperature anomalies associated with positive values of the Asymmetric and Symmetric SAM, respectively. Both the local maximums in the ring and the anomalies in the Pacific regions are present mostly on the Asymmetric SAM regression map, while temperature patterns linked to positive Symmetric SAM show a more zonally consistent ring and less relation to the tropics. Noticeable, temperature anomalies in the Indian ocean, South Africa and Australia are strongly related to Asymmetric SAM. This signal is not present in the regression pattern with the Full SAM. Spring (row 4) features similar patterns but of smaller magnitude, with less regions where regressed anomalies have statistical significance.

In Autumn and Winter (rows 2 and 3) the positive ring is only present through its local maximums in the regression with the Full SAM. There are also negative anomalies in Southern Australia, and positive anomalies over New Zealand and Southern South America. These patterns are not significant in the sense that there are no areas with p-values below 0.05 when controlling for

335 FDR following Wilks (2016). However, repeating this analysis with 2-meter temperature from
336 ERA5 resulted in similar patterns that were statistically significant (not shown). Moreover, similar
337 features were observed in station measurements by Jones et al. (2019), although using data from
338 1957 to 2016.

339 The pattern of negative anomalies in the pole surrounded by positive anomalies roughly seen in all
340 seasons –although with varying intensity and small-scale details– translates to enhanced meridional
341 temperature gradient maximised in the zero line, which is consistent with the intensification and
342 poleward migration of the westerlies commonly linked to the SAM through thermal wind balance.
343 It's then not surprising to see it more clearly in association with the Symmetric SAM (at least in
344 Summer and Spring).

345 Figure 10 column b can be partially compared with Figure 11 from Fogt et al. (2012). Although
346 they used station data from 1958 to 2001, main features are reproduced here, such as the strong
347 signal in New Zealand and Australia in Summer and Spring.

348 Regression of the SAM indices with seasonal mean precipitation and 700 hPa geopotential height
349 are shown in Figures 11 and 12 for Australasia and South America respectively. South Africa is
350 not shown because no significant signal was detected there.

351 In Australia, the annual regression shows that the Full SAM index is positively associated with
352 precipitation in the Southeastern region (Figure 11 panel a.1), which reproduces the results from
353 Gillett et al. (2006). The separation between Asymmetric and Symmetric SAM suggest that
354 this positive anomaly is explained by the Symmetric SAM only in the East coast (panel c.1).
355 Geopotential anomalies associated with this index (black contours) are indicative of easterly flow
356 from the Tasman Sea, which could explain the positive anomalies in precipitation as found by
357 Hendon et al. (2007). The Asymmetric SAM appears related to increased precipitation in the West

358 coast of Southeastern Australia (panel b.2), which could similarly be explained by the anomalous
359 westerly circulation transporting moist air to the continent from the Indian Ocean.

360 The seasonal-level regressions show statistically significant anomalies only in Spring, when
361 positive Full SAM is associated with positive precipitation anomalies in Eastern Australia (panel
362 a.5). In this trimester the Symmetric SAM seems to be associated with precipitation in a relatively
363 reduced area of the East Coast (panel c.5) while the positive precipitation anomalies related with
364 positive Asymmetric SAM affect all Eastern Australia (panel b.5).

365 In Summer, positive Full SAM index is associated with with positive precipitation anomalies in
366 Western and Eastern Australia, particularly in the North East (panel a.2). The Eastern part being
367 dominated by the relationship with the Symmetric SAM and the Western, by the Asymmetric SAM.
368 In Autumn, the regression with Full SAM shows positive values in the North, similar to Summer,
369 and a broad area of positive values in the North-East to South-West direction. This structure seems
370 to be associated with the Symmetric SAM, while the Northern positive values are associated with
371 the Asymmetric SAM. In Winter we see the same NE to SW aligned anomaly (although with much
372 reduced amplitude) that is also present only in relation with the Symmetric SAM. None of these
373 regression coefficients are statistically significant at the 95% level. The Spring signal is broadly
374 consistent with Hendon et al. (2007), but whereas Hendon et al. (2007) also detected a strong signal
375 in Summer, panel a.2 shows no statistically significant association (although the coefficients have
376 the consistent sign).

377 In South America (Figure 12), the annual-level regression shows that positive SAM is associated
378 with statistically significant precipitation decrease in Southeastern South America (SESA) and
379 Southern Chile and non-significant increase in South Brazil, near the South Atlantic Convergence
380 Zone (SACZ) (panel a.1). Panels b.1 and c.1 show a remarkably clean separation between the

381 Asymmetric SAM –associated with the Southeastern South American and Southern Brazilian
382 signals– and the Symmetric SAM –associated with the signal in Southern Chile.

383 Except Winter, seasonal-level regressions mirror this same pattern. Even if not statistically
384 significant, they all show negative values in Southeastern South America and Southern Chile
385 along with positive values in Southern Brazil in relation with the Full SAM. The separation of
386 these features between the Asymmetric SAM and Symmetric SAM regression maps is also rather
387 consistent.

388 The anomalous circulation at 700 hPa associated with the Symmetric SAM (panel c.1) indicate
389 anomalous Easterly flow over Southern Chile. This leads to reduced influx of moist air from the
390 Pacific Ocean which, is the main source of precipitable water in that region (Garreaud 2007). On
391 the other hand, the anomalous circulation associated with positive values of Asymmetric SAM
392 (panel b.1) in the Atlantic is anticyclonic in the South and cyclonic in the North. This creates
393 anomalous South-Easterly flow over Southeastern South America, which inhibits the flow of the
394 Low Level Jet to the region (Silvestri and Vera 2009, Zamboni et al. (2010)). This same pattern
395 was found to be associated with increased precipitation in Southern Brazil during South Atlantic
396 Convergence Zone events (Rosso et al. 2018). There is a small area of increased precipitation with
397 SAM near central Argentina which is also present in the station-based analysis by Gillett et al.
398 (2006) and that is explained by the Asymmetric SAM.

399 *d. Conclusions*

400 In this study we characterise the temporal and spatial variability of the zonally symmetric and
401 asymmetric structure of the SAM. By projecting monthly geopotential fields at each level with
402 the corresponding asymmetric and symmetric pattern, we created two indices for representing the
403 zonally asymmetric and symmetric contributions of the SAM respectively.

As expected, the Asymmetric SAM index correlates strongly with the Symmetric SAM index. In the troposphere, this correlation is maximum at zero lag, while in the stratosphere is maximised with the Asymmetric SAM leading the Symmetric SAM by one month. Since most indices of the SAM are calculated using surface or near-surface conditions, this result would suggest that they might not be sensitive to the most dramatic changes in SAM variability.

The two-year periodicity we found in the stratospheric Symmetric SAM might point to a link between the SAM and the Quasi Biennial Oscillation. There is evidence of influence between the QBO and the Northern Annular Mode (e.g. Holton and Tan 1980, Watson and Gray (2014), Zhang et al. (2020)), so it's not unlikely that the SAM would be similarly connected. However establishing this link would require further research.

We observe a positive trend towards positive SAM in Summer and Autumn, As was documented by previous studies, such as Fogt and Marshall (2020) (and references therein) for surface levels. We show that these trends are maximised at the 100 hPa level and are explained by the zonally symmetric component. We also find a statistically significant positive trend in the Symmetric component of the SAM in the stratosphere that is not apparent in the Full SAM index. In contrast to Fogt et al. (2012) we find some evidence of the SAM becoming more zonally asymmetric, as there is a slight positive trend in the variance explained by the as the Asymmetric SAM explains an increasingly proportion of the total variance.

In the troposphere, the spatial patterns of geopotential associated with the Symmetric SAM are much closer to being truly annular than the patterns associated with the Full SAM index. The Asymmetric SAM, on the other hand, describes a wave-3 pattern with maximum amplitude in the Pacific region and whose phase is rotated a quarter wavelength from the mean zonal wave 3 described by Raphael (2004)'s index. This pattern extends in the troposphere but its maximum

427 is located at 250 hPa, which also could suggest that surface-based indices are not optimum for
428 capturing this variability.

429 This wave-3 pattern is similar to the Pacific-South American Pattern, which is a teleconnection
430 pattern linked to ENSO variability. We found that the significant correlation that exists between
431 the Full SAM index and the Oceanic Niño Index is captured entirely by the Asymmetric SAM
432 index. This suggests that ENSO is linked to SAM exclusively through the variability in the latter's
433 asymmetric component and thus, the Asymmetric SAM index could be a useful measure to further
434 study that relationship.

435 Temperature anomalies associated with the Full SAM broadly show a pattern of negative anoma-
436 lies at polar latitudes surrounded by positive anomalies, but with many deviations from symmetry.
437 The Asymmetric SAM index explains a big portion of these deviations. In particular, the positive
438 phase of the Asymmetric SAM is associated with colder temperatures over Southern Brazil, South
439 Africa and Southern Australia, as well as the negative anomalies in the equatorial Pacific consistent
440 with the ENSO-SAM relationship. These negative anomalies are particularly clear in the DJF
441 and SON trimesters, which include the months in which the ENSO teleconnection is more active
442 (Cazes-Boezio et al. 2003; Fogt et al. 2011; Cai et al. 2020).

443 In Australia the Full SAM is associated with positive precipitation anomalies in South East and
444 this is explained by the Symmetric SAM. However, the Asymmetric SAM is associated with a
445 small area of positive precipitation anomalies in the Eastern Coast of West Australia, maybe due to
446 advection of moist air from the Indian Ocean. In South America, precipitation anomalies associated
447 with the Full SAM are negative both in Southern Chile and Southeastern South America, and
448 positive in Southern Brazil. These features are cleanly separated between the Asymmetric and
449 Symmetric components. The Symmetric SAM explains the negative anomalies in Southern Chile

and the Asymmetric SAM, the negative-positive dipole between Southeastern South America and Southern Brazil. Individual seasons mostly follow this pattern.

Silvestri and Vera (2009) suggests that precipitation impacts linked to the SAM changed rather dramatically before and after 1980. In particular, the negative relationship with precipitation in South America was absent in some areas and switched sign in others in the earlier period. The correlation between ENSO and SAM is similarly non-stationary, also changing sign before the 1980s (Fogt and Bromwich 2006; Clem and Fogt 2013). Seeing as both the ENSO-SAM relationship and most of the precipitation impacts in South America are captured by the Asymmetric SAM, the results presented here are most likely period-dependent.

By successfully separating the zonally symmetric and zonally asymmetric SAM signals, we show that the asymmetric component of the SAM has its unique variability, trends and impacts. This is particularly important in the context of a changing climate, as the impact on the SAM of ozone recovery is modeled as highly zonally symmetric, while the impact of increased concentration of greenhouse gases has also a zonally asymmetric component (Arblaster and Meehl 2006; Simpkins and Karpechko 2012).

Acknowledgments. NOAA Global Surface Temperature (NOAAGlobalTemp) data provided by the NOAA/OAR/ESRL PSL, Boulder, Colorado, USA, from their Web site at <https://psl.noaa.gov/>

The research was supported by UBACyT20020170100428BA and the CLIMAX Project funded by Belmont Forum/ANR-15-JCL/-0002-01. Elio Campitelli was supported by a PhD grant from CONICET, Argentina.

References

Albers, S., and E. Campitelli, 2020: Rsoi: Import Various Northern and Southern Hemisphere Climate Indices.

473 Allaire, J., J. Horner, Y. Xie, V. Marti, and N. Porte, 2019: *Markdown: Render Markdown with*
474 *the c Library 'Sundown'*.

475 Arblaster, J. M., and G. A. Meehl, 2006: Contributions of External Forcings to Southern Annular
476 Mode Trends. *J. Climate*, **19** (12), 2896–2905, doi:10.1175/JCLI3774.1.

477 Baldwin, M. P., 2001: Annular modes in global daily surface pressure. *Geophysical Research*
478 *Letters*, **28** (21), 4115–4118, doi:10.1029/2001GL013564.

479 Baldwin, M. P., and T. J. Dunkerton, 2001: Stratospheric Harbingers of Anomalous Weather
480 Regimes. *Science*, **294** (5542), 581–584, doi:10.1126/science.1063315.

481 Baldwin, M. P., and D. W. J. Thompson, 2009: A critical comparison of stratosphere–troposphere
482 coupling indices. *Quarterly Journal of the Royal Meteorological Society*, **135** (644), 1661–1672,
483 doi:10.1002/qj.479.

484 Baldwin, M. P., and Coauthors, 2001: The quasi-biennial oscillation. *Reviews of Geophysics*,
485 **39** (2), 179–229, doi:10.1029/1999RG000073.

486 Bamston, A. G., M. Chelliah, and S. B. Goldenberg, 1997: Documentation of a highly ENSO-
487 related sst region in the equatorial pacific: Research note. *Atmosphere-Ocean*, **35** (3), 367–383,
488 doi:10.1080/07055900.1997.9649597.

489 Benjamini, Y., and Y. Hochberg, 1995: Controlling the False Discovery Rate: A Practical and
490 Powerful Approach to Multiple Testing. *Journal of the Royal Statistical Society: Series B*
491 *(Methodological)*, **57** (1), 289–300, doi:10.1111/j.2517-6161.1995.tb02031.x.

492 Cai, W., and Coauthors, 2020: Climate impacts of the El Niño–Southern Oscillation on
493 South America. *Nature Reviews Earth & Environment*, **1** (4), 215–231, doi:10.1038/
494 s43017-020-0040-3.

- 495 Campitelli, E., 2020: metR: Tools for Easier Analysis of Meteorological Fields.
- 496 Cazes-Boezio, G., A. W. Robertson, and C. R. Mechoso, 2003: Seasonal Dependence of ENSO
497 Teleconnections over South America and Relationships with Precipitation in Uruguay. *J. Climate*,
498 **16 (8)**, 1159–1176, doi:10.1175/1520-0442(2003)16<1159:SDOETO>2.0.CO;2.
- 499 Chung, C., and S. Nigam, 1999: Weighting of geophysical data in Principal Component
500 Analysis. *Journal of Geophysical Research: Atmospheres*, **104 (D14)**, 16 925–16 928, doi:
501 10.1029/1999JD900234.
- 502 Clem, K. R., and R. L. Fogt, 2013: Varying roles of ENSO and SAM on the Antarctic Peninsula
503 climate in austral spring. *Journal of Geophysical Research: Atmospheres*, **118 (20)**, 11,481–
504 11,492, doi:10.1002/jgrd.50860.
- 505 Dowle, M., and Coauthors, 2020: Data.table: Extension of 'data.frame'.
- 506 Fan, K., 2007: Zonal asymmetry of the Antarctic Oscillation. *Geophysical Research Letters*, **34 (2)**,
507 doi:10.1029/2006GL028045.
- 508 Fogt, R. L., and D. H. Bromwich, 2006: Decadal Variability of the ENSO Teleconnection to
509 the High-Latitude South Pacific Governed by Coupling with the Southern Annular Mode. *J.*
510 *Climate*, **19 (6)**, 979–997, doi:10.1175/JCLI3671.1.
- 511 Fogt, R. L., D. H. Bromwich, and K. M. Hines, 2011: Understanding the SAM influ-
512 ence on the South Pacific ENSO teleconnection. *Clim Dyn*, **36 (7)**, 1555–1576, doi:
513 10.1007/s00382-010-0905-0.
- 514 Fogt, R. L., J. M. Jones, and J. Renwick, 2012: Seasonal Zonal Asymmetries in the Southern
515 Annular Mode and Their Impact on Regional Temperature Anomalies. *J. Climate*, **25 (18)**,
516 6253–6270, doi:10.1175/JCLI-D-11-00474.1.

517 Fogt, R. L., and G. J. Marshall, 2020: The Southern Annular Mode: Variability, trends, and
 518 climate impacts across the Southern Hemisphere. *WIREs Climate Change*, **11** (4), e652, doi:
 519 10.1002/wcc.652.

520 Garreaud, R., 2007: Precipitation and Circulation Covariability in the Extratropics. *J. Climate*,
 521 **20** (18), 4789–4797, doi:10.1175/JCLI4257.1.

522 Gillett, N. P., T. D. Kell, and P. D. Jones, 2006: Regional climate impacts of the Southern Annular
 523 Mode. *Geophysical Research Letters*, **33** (23), doi:10.1029/2006GL027721.

524 Gong, D., and S. Wang, 1999: Definition of Antarctic Oscillation index. *Geophysical Research*
 525 *Letters*, **26** (4), 459–462, doi:10.1029/1999GL900003.

526 Hendon, H. H., D. W. J. Thompson, and M. C. Wheeler, 2007: Australian Rainfall and Surface
 527 Temperature Variations Associated with the Southern Hemisphere Annular Mode. *J. Climate*,
 528 **20** (11), 2452–2467, doi:10.1175/JCLI4134.1.

529 Hersbach, H., and Coauthors, 2020: The ERA5 global reanalysis. *Quarterly Journal of the Royal*
 530 *Meteorological Society*, **146** (730), 1999–2049, doi:10.1002/qj.3803.

531 Ho, M., A. S. Kiem, and D. C. Verdon-Kidd, 2012: The Southern Annular Mode: A comparison of
 532 indices. *Hydrology and Earth System Sciences*, **16** (3), 967–982, doi:10.5194/hess-16-967-2012.

533 Holton, J. R., and H.-C. Tan, 1980: The Influence of the Equatorial Quasi-Biennial Os-
 534 cillation on the Global Circulation at 50 mb. *J. Atmos. Sci.*, **37** (10), 2200–2208, doi:
 535 10.1175/1520-0469(1980)037<2200:TIOTEQ>2.0.CO;2.

536 Hufkens, K., R. Stauffer, and E. Campitelli, 2020: Ecmwfr: Interface to 'ECMWF' and 'CDS'
 537 Data Web Services.

538 Jones, J. M., R. L. Fogt, M. Widmann, G. J. Marshall, P. D. Jones, and M. Visbeck, 2009: Historical
 539 SAM Variability. Part I: Century-Length Seasonal Reconstructions. *J. Climate*, **22** (20), 5319–
 540 5345, doi:10.1175/2009JCLI2785.1.

541 Jones, M. E., D. H. Bromwich, J. P. Nicolas, J. Carrasco, E. Plavcová, X. Zou, and S.-H. Wang, 2019:
 542 Sixty Years of Widespread Warming in the Southern Middle and High Latitudes (1957–2016).
 543 *J. Climate*, **32** (20), 6875–6898, doi:10.1175/JCLI-D-18-0565.1.

544 Karoly, D. J., 1989: Southern Hemisphere Circulation Features Associated with El Niño-Southern
 545 Oscillation Events. *J. Climate*, **2** (11), 1239–1252, doi:10.1175/1520-0442(1989)002<1239:
 546 SHCFAW>2.0.CO;2.

547 Katz, R. W., and B. G. Brown, 1991: The problem of multiplicity in research on teleconnections.
 548 *International Journal of Climatology*, **11** (5), 505–513, doi:10.1002/joc.3370110504.

549 Kidson, J. W., 1988: Interannual Variations in the Southern Hemisphere Circulation. *J. Climate*,
 550 **1** (12), 1177–1198, doi:10.1175/1520-0442(1988)001<1177:IVITSH>2.0.CO;2.

551 Lim, E.-P., H. H. Hendon, J. M. Arblaster, F. Delage, H. Nguyen, S.-K. Min, and M. C. Wheeler,
 552 2016: The impact of the Southern Annular Mode on future changes in Southern Hemisphere
 553 rainfall. *Geophysical Research Letters*, **43** (13), 7160–7167, doi:10.1002/2016GL069453.

554 Marshall, G. J., 2003: Trends in the Southern Annular Mode from Observations and Reanalyses.
 555 *J. Climate*, **16** (24), 4134–4143, doi:10.1175/1520-0442(2003)016<4134:TITSAM>2.0.CO;2.

556 Mo, K. C., and M. Ghil, 1987: Statistics and Dynamics of Persistent Anomalies. *J. Atmos. Sci.*,
 557 **44** (5), 877–902, doi:10.1175/1520-0469(1987)044<0877:SADOPA>2.0.CO;2.

558 R Core Team, 2020: *R: A Language and Environment for Statistical Computing*. Vienna, Austria,
 559 R Foundation for Statistical Computing.

- 560 Raphael, M. N., 2004: A zonal wave 3 index for the Southern Hemisphere. *Geophysical Research*
561 *Letters*, **31 (23)**, doi:10.1029/2004GL020365.
- 562 Rogers, J. C., and H. van Loon, 1982: Spatial Variability of Sea Level Pressure and 500 mb
563 Height Anomalies over the Southern Hemisphere. *Mon. Wea. Rev.*, **110 (10)**, 1375–1392, doi:
564 10.1175/1520-0493(1982)110<1375:SVOSLP>2.0.CO;2.
- 565 Ropelewski, C. F., and P. D. Jones, 1987: An Extension of the Tahiti–Darwin Southern Oscil-
566 lation Index. *Mon. Wea. Rev.*, **115 (9)**, 2161–2165, doi:10.1175/1520-0493(1987)115<2161:
567 AEOTTS>2.0.CO;2.
- 568 Rosso, F. V., N. T. Boiaski, S. E. T. Ferraz, and T. C. Robles, 2018: Influence of the Antarctic
569 Oscillation on the South Atlantic Convergence Zone. *Atmosphere*, **9 (11)**, 431, doi:10.3390/
570 atmos9110431.
- 571 Schneider, U., A. Becker, P. Finger, A. Meyer-Christoffer, B. Rudolf, and M. Ziese, 2015: GPCC
572 Full Data Reanalysis Version 7.0 at 0.5°: Monthly Land-Surface Precipitation from Rain-Gauges
573 built on GTS-based and Historic Data: Gridded Monthly Totals. Global Precipitation Clima-
574 tology Centre (GPCC) at Deutscher Wetterdienst, 20 - 270 MB per decadal gzip compressed
575 NetCDF archive pp., doi:10.5676/DWD_GPCC/FD_M_V7_050.
- 576 Sheather, S. J., and M. C. Jones, 1991: A Reliable Data-Based Bandwidth Selection Method for
577 Kernel Density Estimation. *Journal of the Royal Statistical Society. Series B (Methodological)*,
578 **53 (3)**, 683–690.
- 579 Silvestri, G., and C. Vera, 2009: Nonstationary Impacts of the Southern Annular Mode on Southern
580 Hemisphere Climate. *J. Climate*, **22 (22)**, 6142–6148, doi:10.1175/2009JCLI3036.1.

581 Simpkins, G. R., and A. Y. Karpechko, 2012: Sensitivity of the southern annular mode to green-
582 house gas emission scenarios. *Clim Dyn*, **38** (3), 563–572, doi:10.1007/s00382-011-1121-2.

583 Smith, T. M., R. W. Reynolds, T. C. Peterson, and J. Lawrimore, 2008: Improvements to NOAA’s
584 Historical Merged Land–Ocean Surface Temperature Analysis (1880–2006). *J. Climate*, **21** (10),
585 2283–2296, doi:10.1175/2007JCLI2100.1.

586 Vose, R. S., and Coauthors, 2012: NOAA’s Merged Land–Ocean Surface Temperature Analysis.
587 *Bull. Amer. Meteor. Soc.*, **93** (11), 1677–1685, doi:10.1175/BAMS-D-11-00241.1.

588 Walker, S. G. T., 1914: *Correlation in Seasonal Variations of Weather, III: On the Criterion for*
589 *the Reality of Relationships Or Periodicities*. Meteorological Office.

590 Watson, P. A. G., and L. J. Gray, 2014: How Does the Quasi-Biennial Oscillation Affect the
591 Stratospheric Polar Vortex? *J. Atmos. Sci.*, **71** (1), 391–409, doi:10.1175/JAS-D-13-096.1.

592 Wickham, H., 2009: *Ggplot2: Elegant Graphics for Data Analysis*. Use R!, Springer-Verlag, New
593 York, doi:10.1007/978-0-387-98141-3.

594 Wilks, D. S., 2016: “The Stippling Shows Statistically Significant Grid Points”: How Research
595 Results are Routinely Overstated and Overinterpreted, and What to Do about It. *Bull. Amer.*
596 *Meteor. Soc.*, **97** (12), 2263–2273, doi:10.1175/BAMS-D-15-00267.1.

597 Wolter, K., and M. S. Timlin, 2011: El Niño/Southern Oscillation behaviour since 1871 as diag-
598 nosed in an extended multivariate ENSO index (MEI.ext). *International Journal of Climatology*,
599 **31** (7), 1074–1087, doi:10.1002/joc.2336.

600 Xie, Y., 2015: *Dynamic Documents with R and Knitr*. 2nd ed., Chapman and Hall/CRC, Boca
601 Raton, Florida.

602 Zamboni, L., C. R. Mechoso, and F. Kucharski, 2010: Relationships between Upper-Level Circu-
603 lation over South America and Rainfall over Southeastern South America: A Physical Base for
604 Seasonal Predictions. *J. Climate*, **23** (12), 3300–3315, doi:10.1175/2009JCLI3129.1.

605 Zhang, R., W. Tian, and T. Wang, 2020: Role of the quasi-biennial oscillation in the downward
606 extension of stratospheric northern annular mode anomalies. *Clim Dyn*, **55** (3), 595–612, doi:
607 10.1007/s00382-020-05285-4.

608

APPENDIX

609

Extra figures

610	LIST OF FIGURES	
611	Fig. 1. Spatial patterns of the first EOF of 700 hPa geopotential height for 1979-2018 period	33
612	Fig. 2. Time series for the Asymmetric SAM and Symmetric SAM indices at (a) 50 hPa and (b) 700	
613	hPa	34
614	Fig. 3. Correlation between the Symmetric SAM and Asymmetric SAM index at each level for lag	
615	zero and lag -1 (Asymmetric SAM leads Symmetric SAM) for the 1979-2018 period	35
616	Fig. 4. Cross correlation between levels of the (a) Full SAM, (b) Asymmetric SAM, and (c) Sym-	
617	metric SAM for the 1979-2018 period	36
618	Fig. 5. Decadal linear trends at each level for annual (row 1) and seasonal values (rows 2 to 5) for	
619	the period 1979-2018 and for the (column a) Full SAM index, (column b) Asymmetric SAM	
620	index, and (column c) Symmetric SAM index	37
621	Fig. 6. Decadal trends of the variance explained by the Asymmetric and Symmetric SAM at each	
622	level for the period 1979-2018	38
623	Fig. 7. Regression of geopotential height (meters) at (row 1) 50 hPa and (row 2) 700 hPa with the	
624	(column a) Full SAM, (column b) Asymmetric SAM, and (column c) Symmetric SAM for	
625	the 1979-2018 period	39
626	Fig. 8. Amplitude (meters) of zonal waves of the geopotential height regression patterns in Figure	
627	7 for zonal waves with wave-number 0, 1, 2, and 3, where wave-number 0 represents the	
628	amplitude of the zonal mean.	40
629	Fig. 9. Regression between monthly geopotential height anomalies (meters) averaged between	
630	65° and 40°S and the Asymmetric SAM index (extracted from multiple regression including	
631	the Symmetric SAM)	41
632	Fig. 10. Regression of seasonal mean surface temperature (Kelvin) with Asymmetric SAM and	
633	Symmetric SAM for the 1979-2018 period	42
634	Fig. 11. Regression of (row 1) annual and (rows 2 to 5) seasonal mean precipitation anomalies (mm	
635	per day, shading) and 700 hPa geopotential height (thin lines, positive values as solid lines	
636	and negative values as dashed lines) with (column a) Full SAM, (column b) Asymmetric	
637	SAM and (column c) Symmetric SAM for the 1979-2018 period	43
638	Fig. 12. Same as Figure 11 but for South America.	44
639	Fig. A1. Lag-correlation between Asymmetric SAM and Symmetric SAM index at each level. Neg-	
640	ative lags imply Symmetric SAM leading Asymmetric SAM and vice versa.	45
641	Fig. A3. Fourier spectrum of each timeseries computed as Fourier transform smoothed with modified	
642	Daniell smoothers with widths 3 and 5. The shading indicates the 95% confidence area derived	
643	by fitting an autoregressive model and computing the spectrum for 5000 simulated samples	
644	from the fitted autoregressive model (95% of the simulated samples had an amplitude equal	
645	or lower). The light line indicates the theoretical expected amplitude from the autoregressive	
646	model.	46

647	Fig. 13.	700 hPa Geopotetnial height zonal anomalies (meters) of composites of positive and negative	
648		SAM months selected using ± 1 standard deviation as threshold	47
649	Fig. 14.	Regression of 700 hPa geopotential height zonal anomalies (meters) onto the standarised	
650		timeseries of the leading EOF computed for each season independently	48
651	Fig. 15.	Regression of 700 hPa geopotential height zonal anomalies (meters) onto the standarised	
652		timeseries of the leading EOF computed for the periods 1979 to 1998 and 1999 to 2018	49

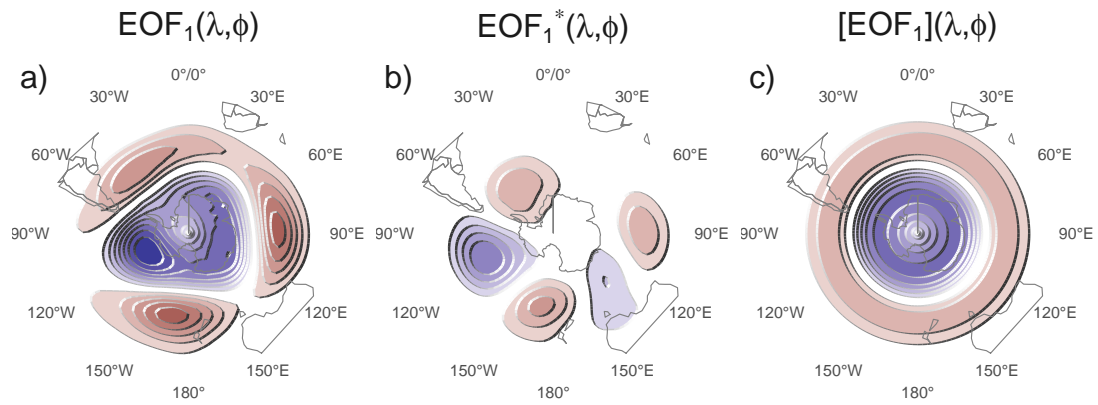


FIG. 1: Spatial patterns of the first EOF of 700 hPa geopotential height for 1979-2018 period. (a) Full field, (b) zonally asymmetric component and (c) zonally symmetric component. Arbitrary units.

fig:method

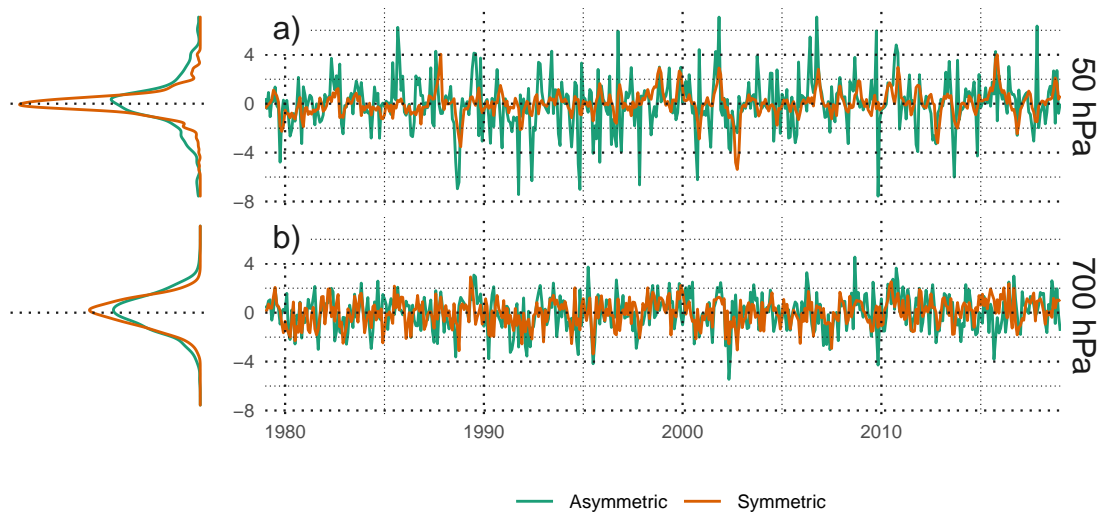


FIG. 2: Time series for the Asymmetric SAM and Symmetric SAM indices at (a) 50 hPa and (b) 700 hPa. To the left, probability density estimate of each index computed using a gaussian kernel of optimal bandwidth according to Sheather and Jones (1991). Series are standardised by the standard deviation of the Full SAM at each level.

fig:asysam-timeseries

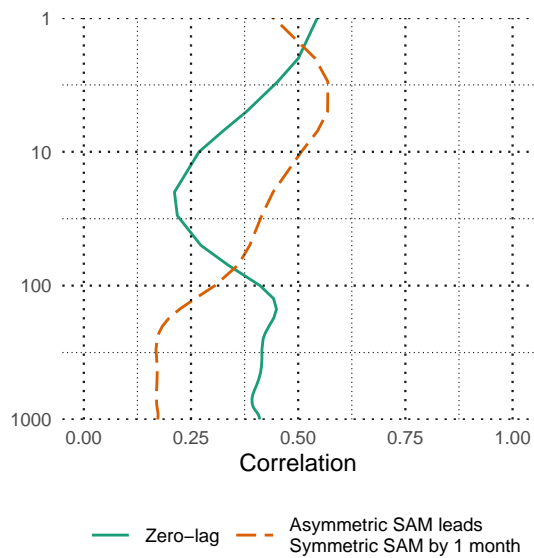


FIG. 3: Correlation between the Symmetric SAM and Asymmetric SAM index at each level for lag zero and lag -1 (Asymmetric SAM leads Symmetric SAM) for the 19792018 period.

fig:cor-lev

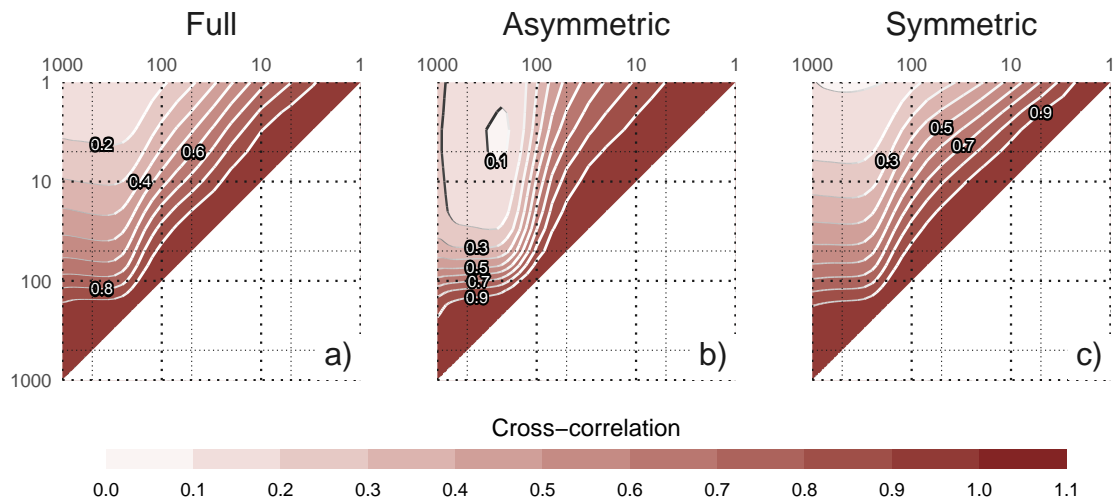


FIG. 4: Cross correlation between levels of the (a) Full SAM, (b) Asymmetric SAM, and (c) Symmetric SAM for the 1979-2018 period.

fig:cross-correlation

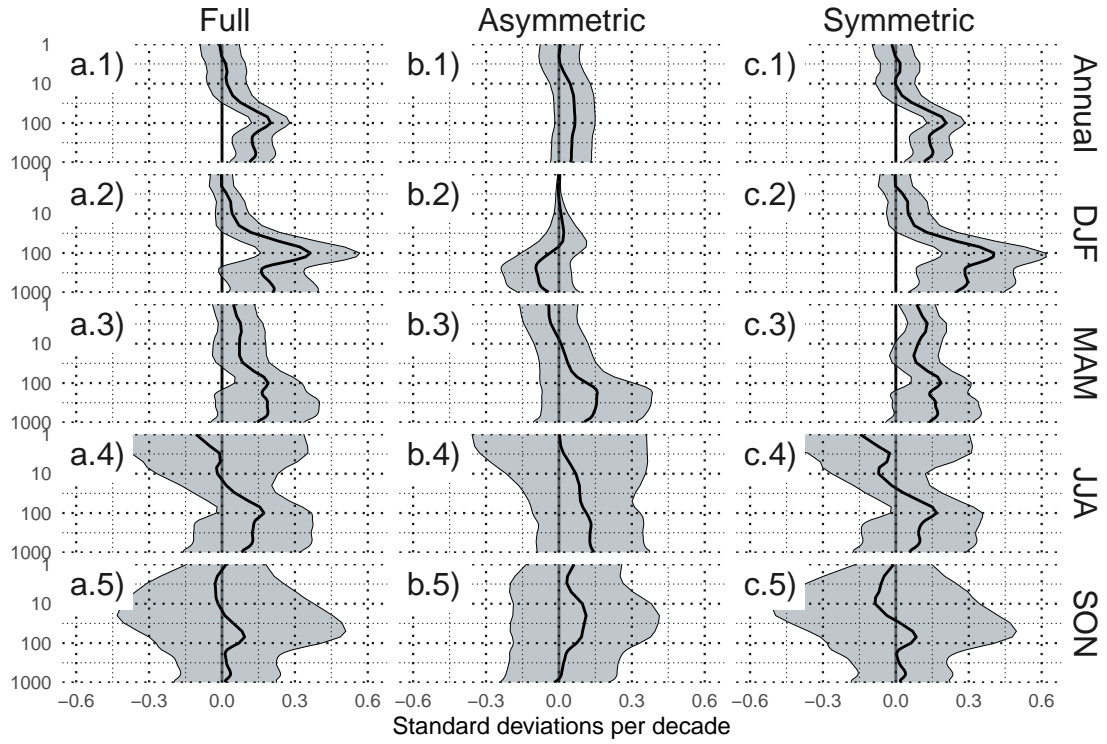


FIG. 5: Decadal linear trends at each level for annual (row 1) and seasonal values (rows 2 to 5) for the period 1979-2018 and for the (column a) Full SAM index, (column b) Asymmetric SAM index, and (column c) Symmetric SAM index. Shading indicates the 95% confidence interval from a t-distribution.

fig:trends

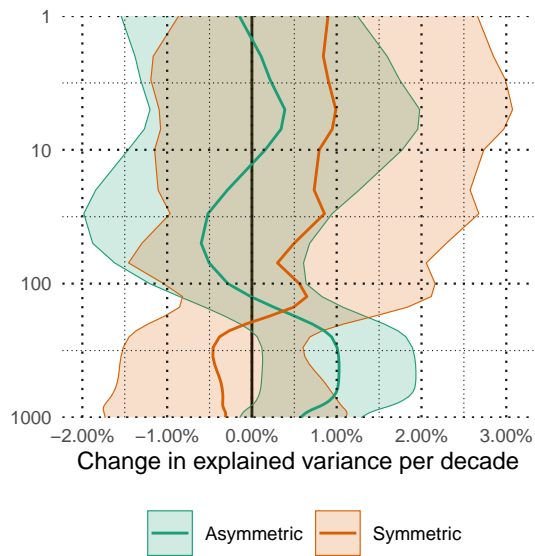


FIG. 6: Decadal trends of the variance explained by the Asymmetric and Symmetric SAM at each level for the period 1979-2018. Shading indicates the 95% confidence interval.

fig:r-squared-trend

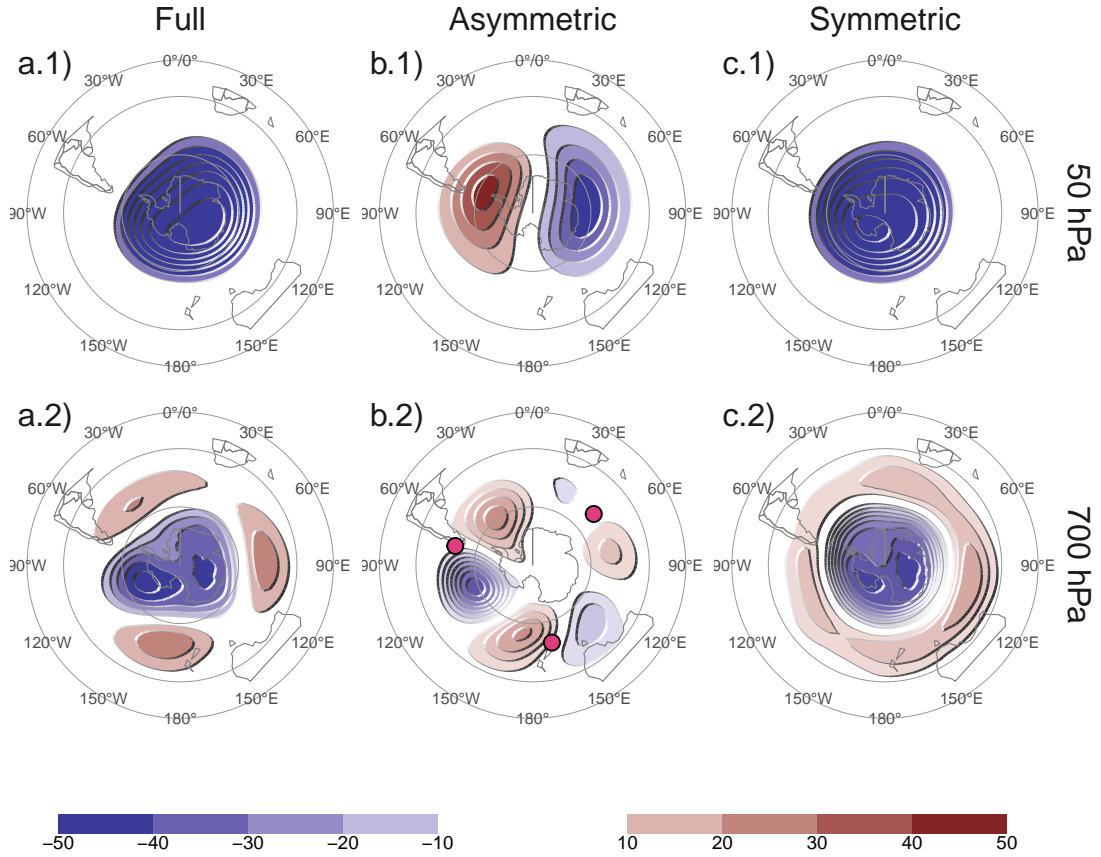


FIG. 7: Regression of geopotential height (meters) at (row 1) 50 hPa and (row 2) 700 hPa with the (column a) Full SAM, (column b) Asymmetric SAM, and (column c) Symmetric SAM for the 1979-2018 period. The regression patterns for Asymmetric and Symmetric SAM are the result of one multiple regression using both indices. Points marked on panel b.2 are the location of the reference points used by Raphael (2004) for their Zonal Wave 3 index.

fig:2d-regr

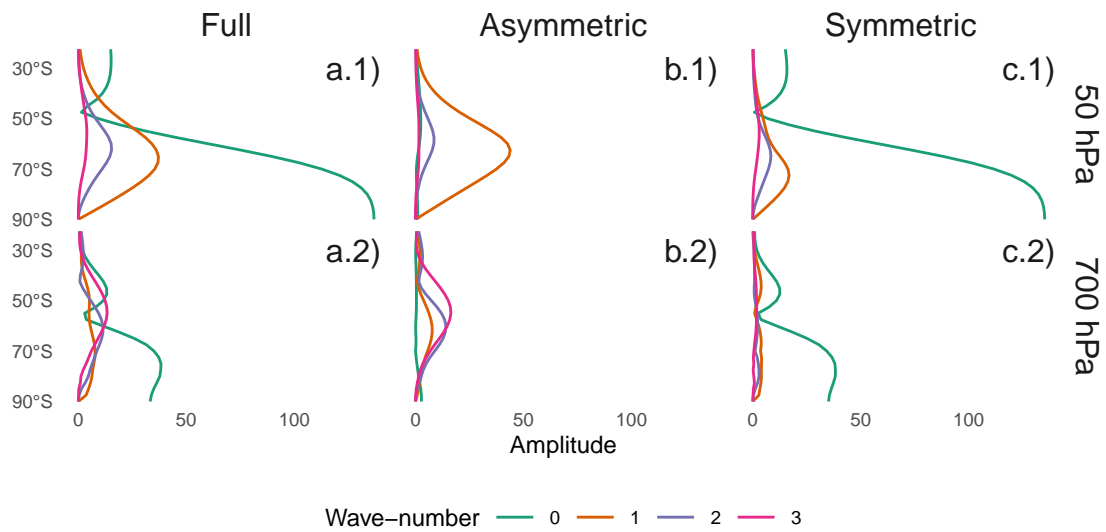


FIG. 8: Amplitude (meters) of zonal waves of the geopotential height regression patterns in Figure 7 for zonal waves with wave-number 0, 1, 2, and 3, where wave-number 0 represents the amplitude of the zonal mean.

fig:wave-amplitude

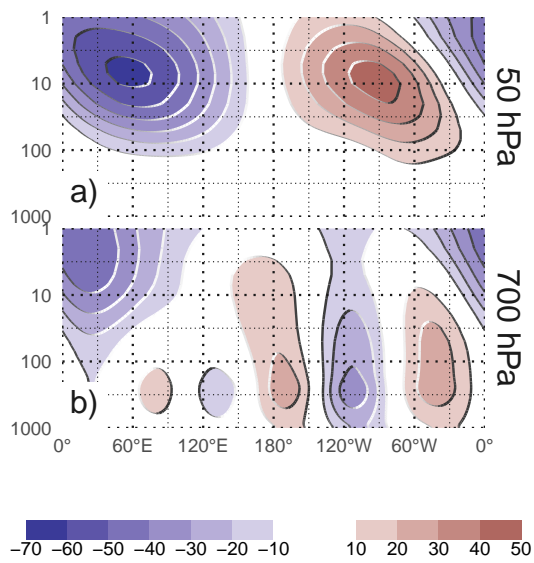


FIG. 9: Regression between monthly geopotential height anomalies (meters) averaged between 65° and 40°S and the Asymmetric SAM index (extracted from multiple regression including the Symmetric SAM). (a) With the Asymmetric SAM in 50 hPa and (b) in 700 hPa for the 1979-2018 period.

fig:vertical-regression

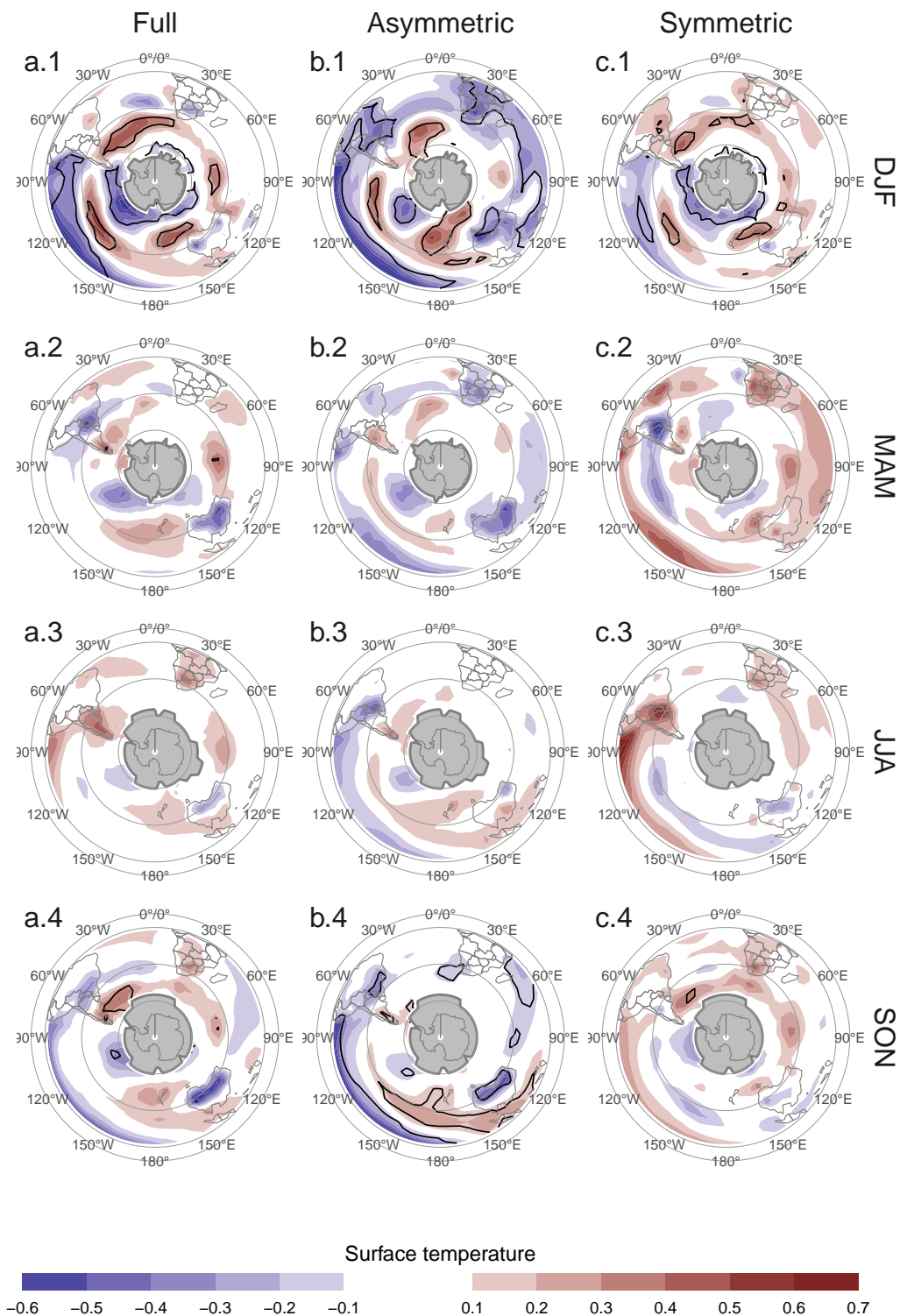


FIG. 10: Regression of seasonal mean surface temperature (Kelvin) with Asymmetric SAM and Symmetric SAM for the 1979-2018 period. Black contours indicate areas with p-value smaller than 0.05 controlling for False Detection Rate. Gray areas in Antarctica are areas with have more than 15% of missing data.

fig:regr-air-season

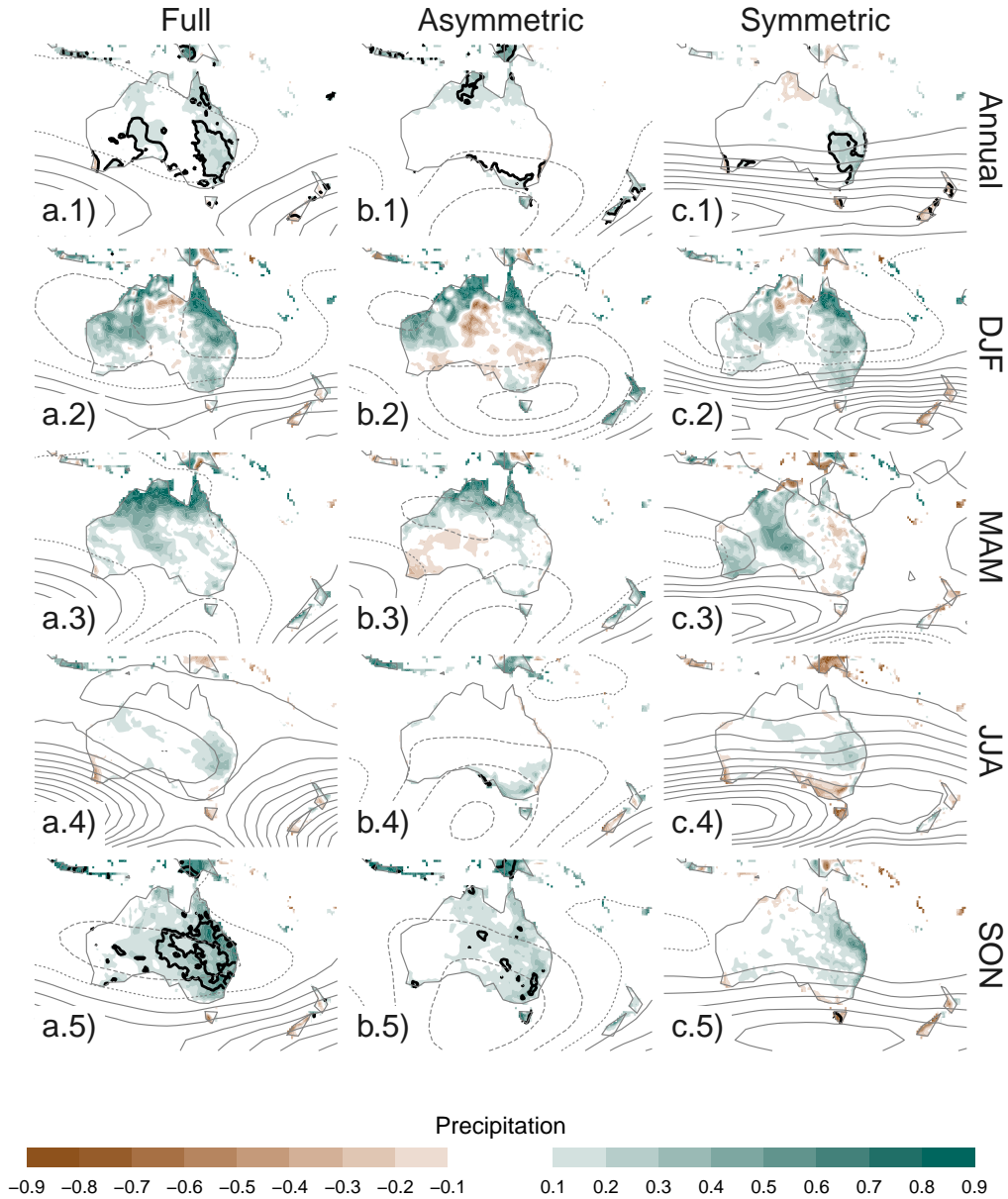


FIG. 11: Regression of (row 1) annual and (rows 2 to 5) seasonal mean precipitation anomalies (mm per day, shading) and 700 hPa geopotential height (thin lines, positive values as solid lines and negative values as dashed lines) with (column a) Full SAM, (column b) Asymmetric SAM and (column c) Symmetric SAM for the 1979-2018 period. Thin lines are the Black contours indicate areas with p-value smaller than 0.05 controlling for False Detection Rate.

fig:pp-regr-oceania

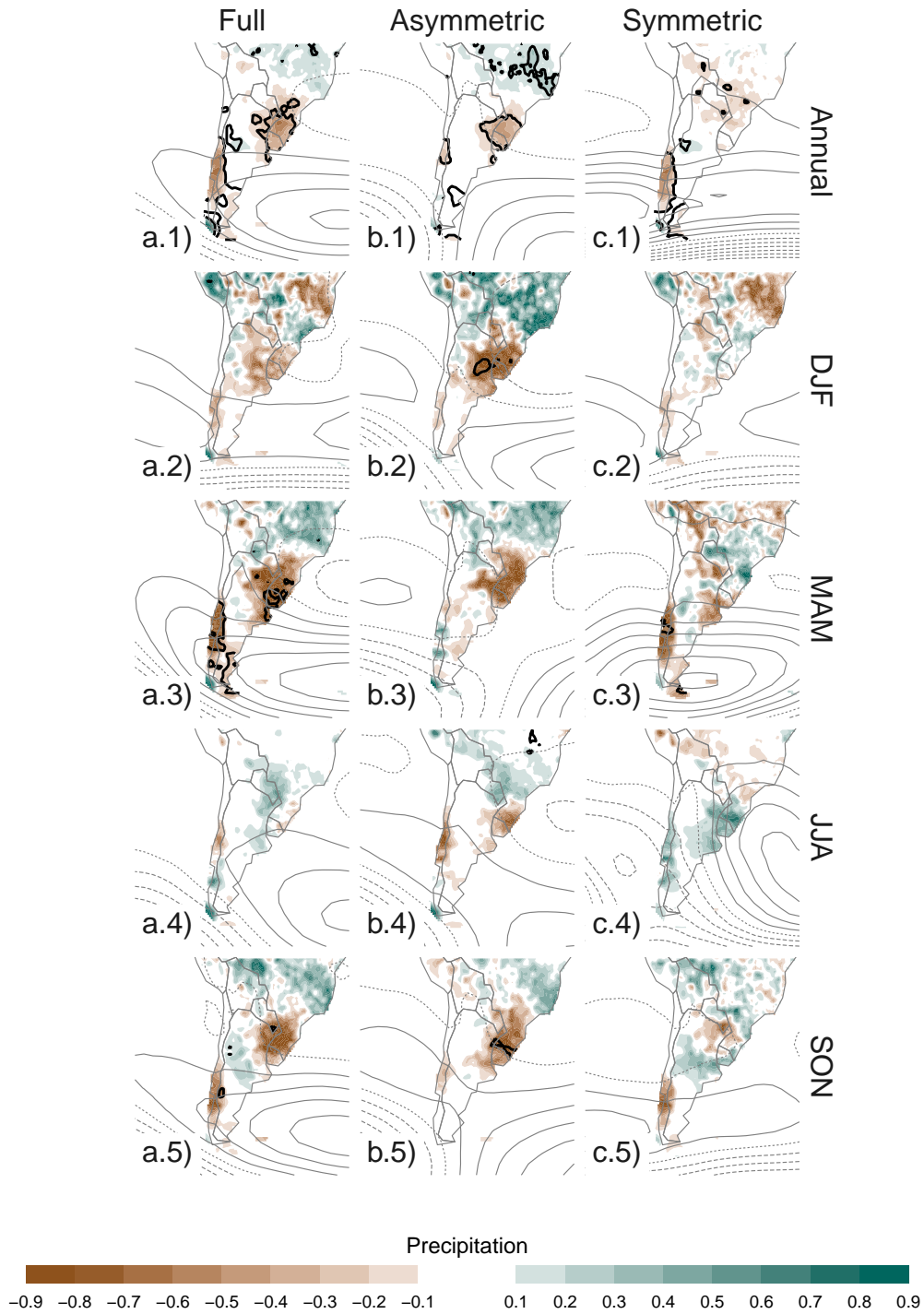


FIG. 12: Same as Figure 11 but for South America.

fig:pp-regr-america

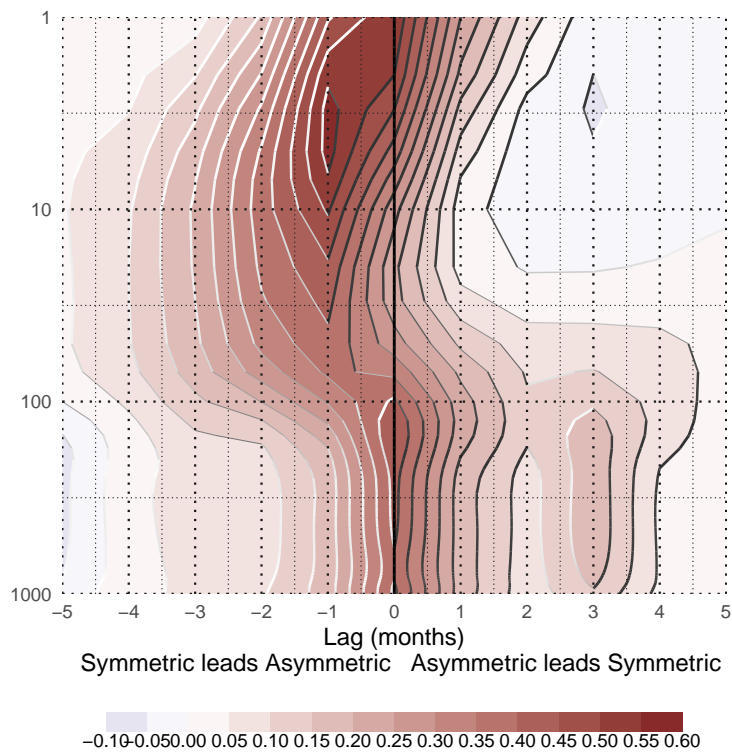


Fig. A1: Lag-correlation between Asymmetric SAM and Symmetric SAM index at each level. Negative lags imply Symmetric SAM leading Asymmetric SAM and vice versa.

fig:A1

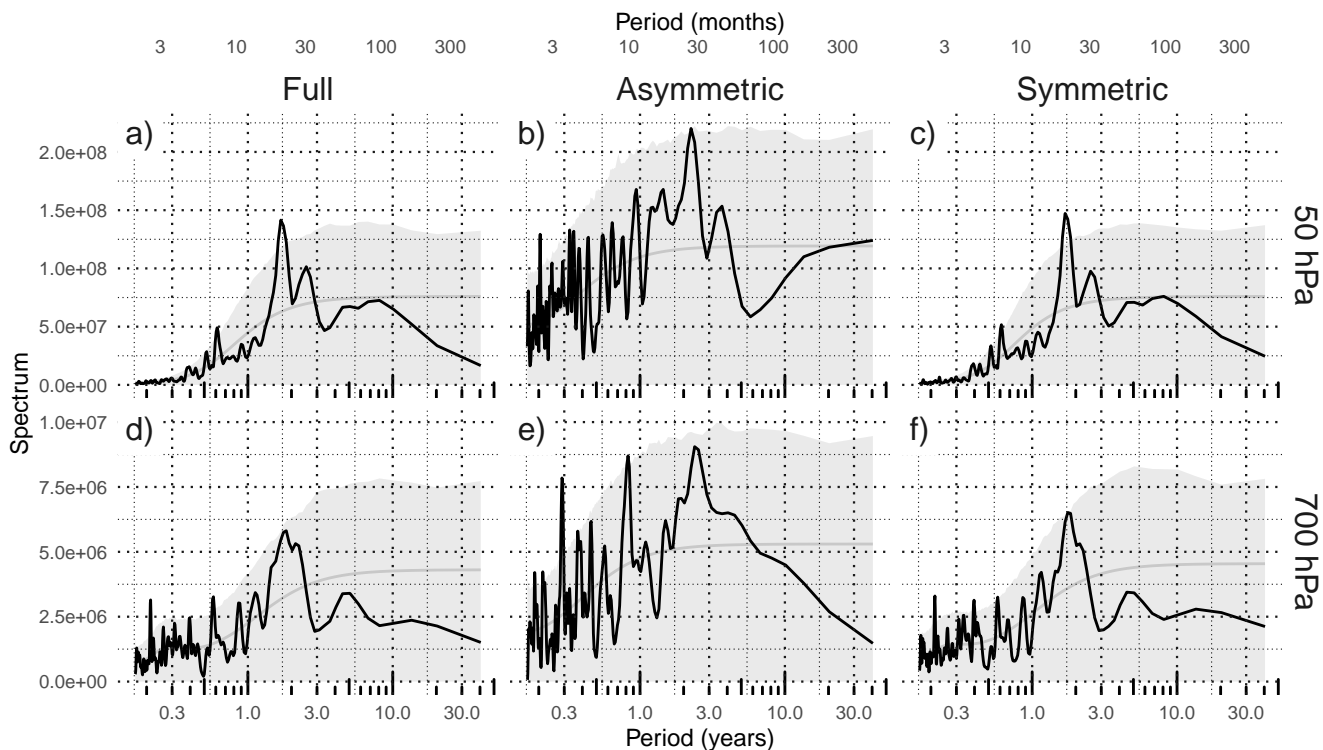


Fig. A3: Fourier spectrum of each timeseries computed as Fourier transform smoothed with modified Daniell smoothers with widths 3 and 5. The shading indicates the 95% confidence area derived by fitting an autoregressive model and computing the spectrum for 5000 simulated samples from the fitted autoregressive model (95% of the simulated samples had an amplitude equal or lower). The light line indicates the theoretical expected amplitude from the autoregressive model.

fig:A3

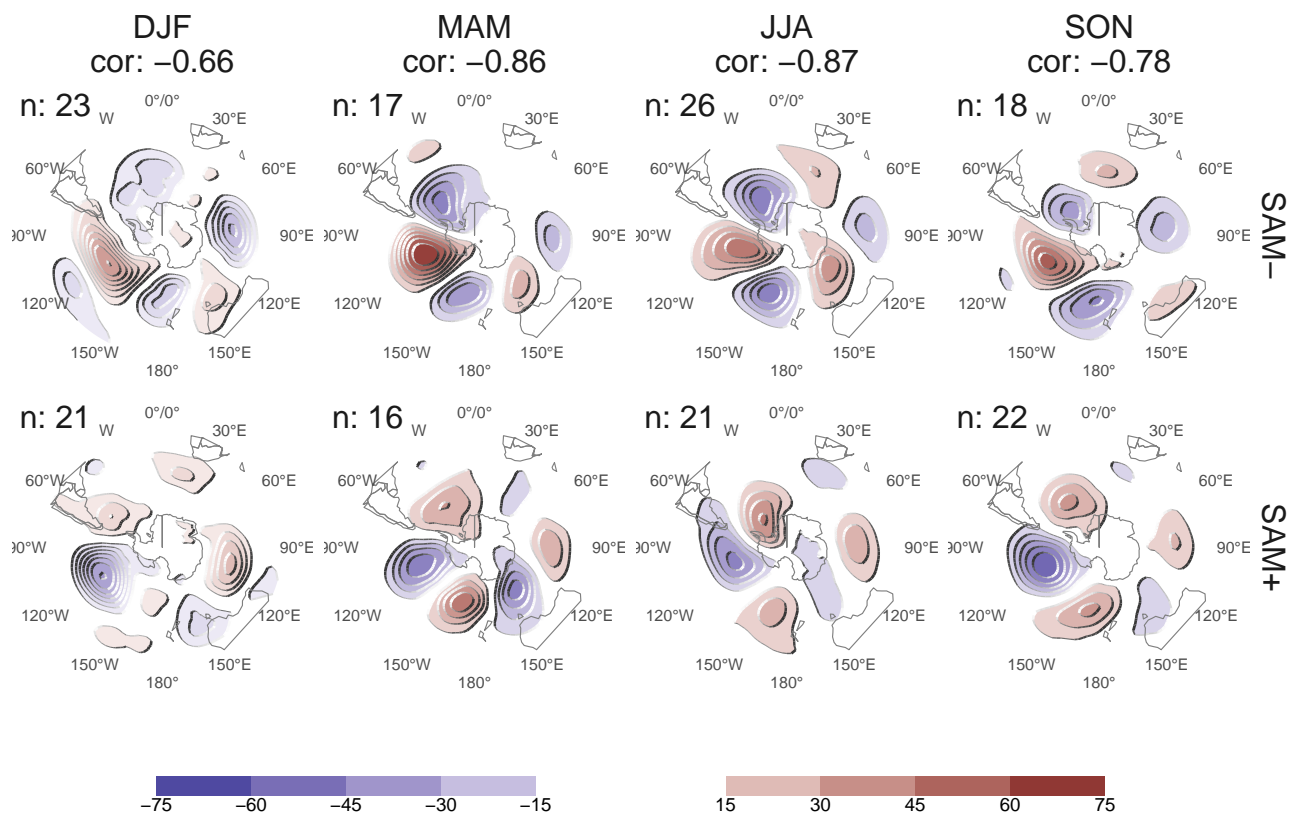


FIG. 13: 700 hPa Geopotential height zonal anomalies (meters) of composites of positive and negative SAM months selected using ± 1 standard deviation as threshold. Numbers in the column headers are pattern correlation between SAM+ and SAM- composites and number of monthly fields used to construct the composites.

fig:A9

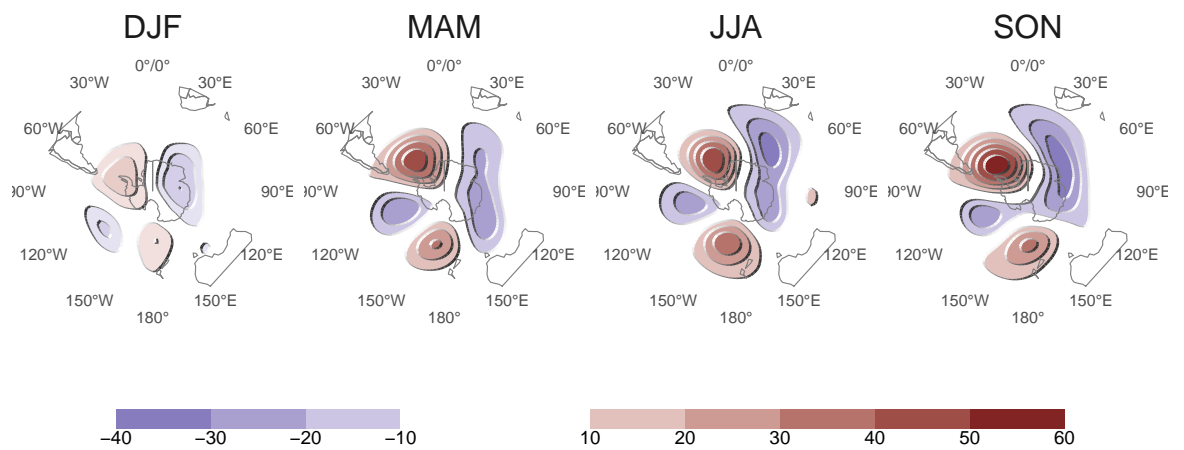


FIG. 14: Regression of 700 hPa geopotential height zonal anomalies (meters) onto the standardised timeseries of the leading EOF computed for each season independently.

fig:A10

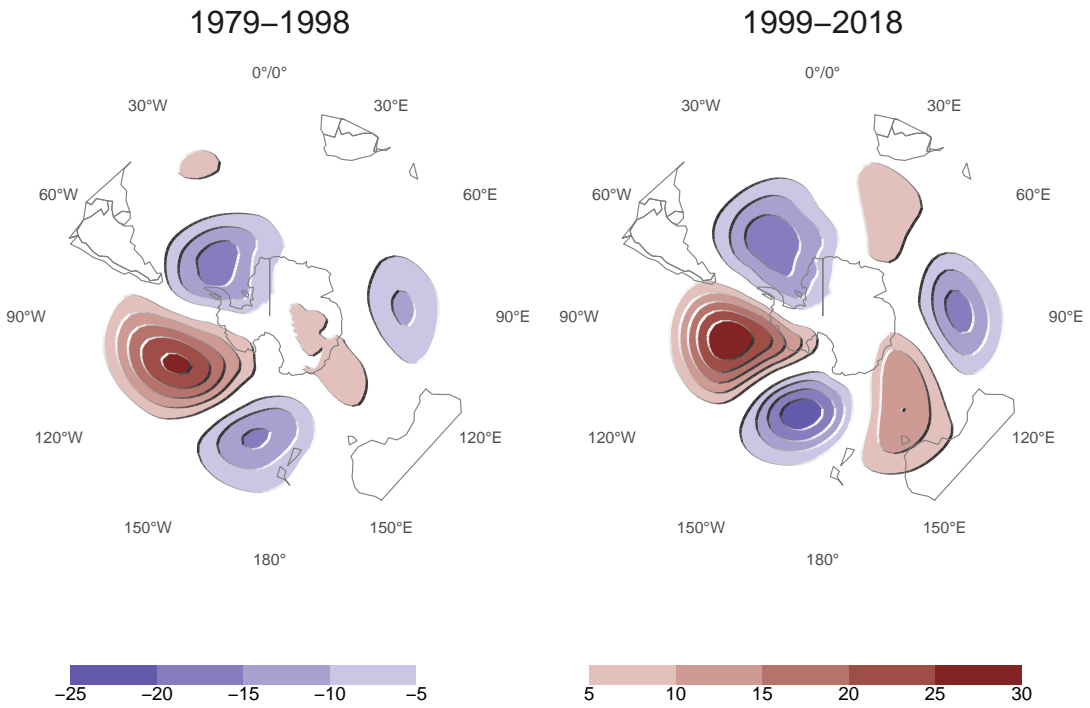


FIG. 15: Regression of 700 hPa geopotential height zonal anomalies (meters) onto the standardised timeseries of the leading EOF computed for the periods 1979 to 1998 and 1999 to 2018. Pattern correlation between both fields is 0.76.

fig:A11